The Astrophysical Journal, 746:174 (15pp), 2012 February 20 doi:10.1088/0004-637X/746/2/174

VERY LARGE ARRAY OBSERVATIONS OF AMMONIA IN INFRARED-DARK CLOUDS. II. INTERNAL KINEMATICS

Sarah E. Ragan[1,2], Fabian Heitsch[3], Edwin A. Bergin[1], and David Wilner[4]
[1] Department of Astronomy, University of Michigan, 830 Dennison Building, 500 Church Street, Ann Arbor, MI 48109, USA
[2] Max Planck Institute for Astronomy, Königstuhl 17, 69117 Heidelberg, Germany; ragan@mpia.de
[3] Department of Physics and Astronomy, University of North Carolina-Chapel Hill, CB 3255 Phillips Hall, Chapel Hill, NC 27599, USA
[4] Smithsonian Center for Astrophysics, Mail Stop 42, 60 Garden Street, Cambridge, MA 02138, USA
Received 2011 May 31; accepted 2012 January 5; published 2012 February 3

ABSTRACT

Infrared-dark clouds (IRDCs) are believed to be the birthplaces of rich clusters and thus contain the earliest phases of high-mass star formation. We use the Green Bank Telescope and Very Large Array maps of ammonia (NH_3) in six IRDCs to measure their column density and temperature structure (Paper 1), and here, we investigate the kinematic structure and energy content. We find that IRDCs overall display organized velocity fields, with only localized disruptions due to embedded star formation. The local effects seen in NH_3 emission are not high-velocity outflows but rather moderate (few km s^{-1}) increases in the linewidth that exhibit maxima near or coincident with the mid-infrared emission tracing protostars. These linewidth enhancements could be the result of infall or (hidden in NH_3 emission) outflow. Not only is the kinetic energy content insufficient to support the IRDCs against collapse, but also the spatial energy distribution is inconsistent with a scenario of turbulent cloud support. We conclude that the velocity signatures of the IRDCs in our sample are due to active collapse and fragmentation, in some cases augmented by local feedback from stars.

Key words: Galaxy: structure – ISM: clouds – ISM: kinematics and dynamics – radio lines: ISM – stars: formation – techniques: interferometric – techniques: spectroscopic

Online-only material: color figures

1. INTRODUCTION

Star formation has been the focus of observational and theoretical studies for decades, but still the conditions under which this process commences are quite uncertain. The identification of objects in different evolutionary stages, such that a sequence can be constructed, is the essential observational ingredient needed to test theoretical scenarios. In the solar neighborhood, it is possible to resolve the precursors to stars (or multiple systems), known as pre-stellar cores, but the counterpart in massive regions has to date been difficult to isolate. With the recent surveys by *Spitzer* in the mid-infrared and advancement of millimeter and radio interferometric arrays, progress in identifying objects in various early phases of massive star formation has been rapid.

Infrared-dark clouds (IRDCs), the densest parts of molecular cloud complexes embedded within Galactic spiral arms (Jackson et al. 2008), are believed to host these earliest stages of clustered star formation. Studies in the infrared (e.g., Perault et al. 1996; Egan et al. 1998; Ragan et al. 2009; Butler & Tan 2009; Peretto & Fuller 2009), millimeter continuum (e.g., Rathborne et al. 2006; Vasyunina et al. 2009), and molecular lines (e.g., Carey et al. 1998, 2000; Ragan et al. 2006; Pillai et al. 2006; Sakai et al. 2008; Du & Yang 2008) have shown that IRDCs contain from tens to thousands of solar masses of dense ($N(H_2) \sim 10^{22-23}$ cm^{-2}) material and have the right physical conditions ($T < 15$ K, $n > 10^5$ cm^{-3}) to give rise to rich star clusters, i.e., clusters which can potentially host massive ($M > 10\,M_\odot$) stars.

Star formation is dynamical by nature (see McKee & Ostriker 2007 for a review of the important processes), but observational tests of dynamics are complicated by the projection of this three-dimensional process onto the two-dimensional plane of the sky. Molecular line emission—from a number of molecules excited in the cold environments of molecular clouds—is the key tool to help disentangle the problem along the line of sight. Ammonia (NH_3) has been a particularly useful probe in molecular clouds (Ho & Townes 1983), as it not only provides kinematic information but also serves as a cloud thermometer (Walmsley & Ungerechts 1983; Maret et al. 2009). Ammonia has been used widely to study local clouds (e.g., Myers & Benson 1983; Ladd et al. 1994; Wiseman & Ho 1998; Jijina et al. 1999; Rosolowsky et al. 2008; Friesen et al. 2009) and IRDCs (e.g., Pillai et al. 2006; Devine et al. 2011). These studies focus on the lower metastable states, $(J, K) = (1,1)$ and (2,2), sensitive to the coldest (<20 K) gas without any evidence of depletion.

In Ragan et al. (2011, hereafter Paper 1), we detailed Very Large Array (VLA) observations mapping six IRDCs in the NH_3 $(J, K) = (1,1)$ and (2,2). We used the maps to produce column density and gas temperature profiles. With between 4″ and 8″ angular resolution, we find that ammonia traces the absorbing structure seen at 8 and 24 μm with *Spitzer* (Ragan et al. 2009), and there is no evidence of depletion of ammonia in IRDCs. We estimated a total ammonia abundance of 8.1×10^{-7} and found that the gas temperature is roughly constant, between 8 and 13 K, across the clouds. Here, we further our analysis of these ammonia data, focusing on the velocity structure of the clouds. The high angular resolution allows us to profile the kinematics and examine their dynamical state and stability.

2. DATA AND METHODS

We obtained observations of the NH_3(1,1) and (2,2) inversion transitions with the Green Bank Telescope (GBT) and VLA. The observations are described in detail in Paper 1. The single-dish and interferometer data were combined in MIRIAD (a full description of the method is found in Paper 1). A summary of the target properties sensitivity and resolution of the combined

Table 1
Target Summary

IRDC	R.A. (J2000)	Decl. (J2000)	Distance[a] (kpc)	v_{lsr} (km s^{-1})	rms[b] (mJy)	Beam Size ($'' \times ''$)	M_{IRDC}[c] ($10^3\ M_\odot$)	Area (pc^2)	B_{cr}[d] (mG)
G005.85−0.23	17:59:51.4	−24:01:10	3.14	17.2	2.8	7.7 × 6.8	5.5	0.55	1.63
G009.28−0.15	18:06:50.8	−21:00:25	4.48	41.4	4.8	8.3 × 6.4	1.8	1.8	1.43
G009.86−0.04	18:07:35.1	−20:26:09	2.36	18.1	4.3	8.1 × 6.3	2.6	1.3	0.87
G023.37−0.29	18:34:54.1	−08:38:21	4.70	78.5	2.5	5.7 × 3.7	10.9	4.4	1.05
G024.05−0.22	18:35:54.4	−07:59:51	4.82	81.4	4.3	8.2 × 7.0	4.0	1.8	0.99
G034.74−0.12	18:55:09.5	+01:33:14	4.86	79.1	6.8	8.1 × 7.0	5.5	1.6	1.43

Notes.
[a] Assume the kinematic "near" distances from Ragan et al. (2006).
[b] rms of the combined data set.
[c] From absorption at 8 μm (Ragan et al. 2009).
[d] Critical field strength, see Section 4.3 and Equation (8).

data set is given in Table 1. The combined data set has a velocity resolution of 0.6 km s^{-1}. In Table 1, we also list the estimated mass and cloud area based on 8 μm extinction, which was computed with *Spitzer* data in Ragan et al. (2009) and the critical magnetic field strength required for support, which will be discussed in Section 4.3.

At each position, the ammonia spectra were fit with a custom Gaussian fitting algorithm utilizing the IDL procedure `gaussfit`. The configuration we used for the VLA back end did not fit the entire NH_3(1,1) hyperfine signature (spanning ∼3.6 MHz) in the bandpass (3.125 MHz). Our line-fitting routine takes a "first guess" line-center velocity of the central line (from Ragan et al. 2006; see Table 1) which is offset by approximately 7.7 km s^{-1} from the neighboring hyperfine components to either side. We fit each of the components independently. For the NH_3(2,2) lines, a single Gaussian was fit to the line independently of the results of the (1,1) fit. From these fits, we extract the peak intensity, line-center velocity, and Gaussian width of the lines at each position.

3. RESULTS

Figures 1–6 show the NH_3(1,1) integrated intensity[5] and (2,2) integrated intensity plotted over the 8 and 24 μm *Spitzer* images of the regions (from Ragan et al. 2009), respectively, and maps of the line-center velocity (first moment) and linewidth (second moment) for the central component of the NH_3(1,1) signature. We also plot the physical scale assuming the distances in Table 1.

3.1. Properties of Individual Sources

Paper 1 demonstrates that the gas in these IRDCs exhibits uniform temperatures, changing by only a few Kelvin in a given object, not significantly more than the error. In contrast, their velocity fields—both the line-center velocities and linewidth measurements—show a connection between the presence of embedded star formation activity and complex kinematic signatures. The upper panels of Figures 1–6 show the (zeroth, first, and second, from left to right) moment maps derived from the NH_3(1,1) observations for each IRDC in the sample with symbols indicating the locations of the 24 μm point sources and other young stars, and the lower panels show the same for the NH_3(2,2) emission. Table 2 summarizes the kinematic properties of the emission peaks. Although we list only the velocity properties of the central component of the NH_3(1,1) line, the velocity structure traced by the satellite lines closely follows the trends seen in the central line. We also list the main line optical depth of the NH_3(1,1) transition, τ_m(1,1), the ratio of thermal to non-thermal contributions to the pressure (R_p), which will be discussed in Section 4, and notes about the velocity trend in the cloud or particular characteristics of the integrated intensity peak. In this section, we discuss the centroid velocity and linewidth trends in each IRDC individually and connect the detected 24 μm point sources to the kinematic signatures.

For the sake of our modeling, we categorize each IRDC based on its NH_3(1,1) emission morphology as either a "sphere" for objects with an aspect ratio, r, close to one or a "filament" for objects with r much greater than one. The axes used to make this distinction are indicated in Figures 1–6, and the morphological type is listed in Table 1. For spheres, the aspect ratio is no greater than 1.1, and the elongated structures, or "filaments," range from 1.6 to 2.9 in r.

G005.85−0.23. This source appears approximately round ($r \sim 1.1$) in the NH_3(1,1) and (2,2) integrated intensity map. The peak at $\alpha(2000) = 17^h59^m51\overset{s}{.}4$, $\delta(2000) = -24°01'10''$ corresponds to the position of the peak in 8 μm optical depth. There are no 24 μm sources in the mapped region.

The smooth gradient in centroid velocity in this IRDC permits us to straightforwardly quantify and distinguish the large-scale ordered motions and the remaining residual motion on small scales. We show in the central panels of Figure 1 a clear velocity gradient oriented 30° east of north. The total gradient in the NH_3(1,1) emission is 1.2 km s^{-1} over 35 arcsec, or 0.5 pc, resulting in a velocity gradient of 2.4 km s^{-1} pc^{-1}. If this linear gradient is subtracted, the residual values do no exceed 0.2 km s^{-1}, indicating the bulk motion dominates the dynamics of the cloud. The overall linewidth measured across the cloud is very low, between 1.3 and 1.8 km s^{-1}, but it increases sharply at the edges (to ∼3 km s^{-1}) where the centroid velocity also falls off quickly.

G009.28−0.15. In this "filament" ($r \sim 1.6$), there are three integrated intensity maxima: the central peak ($\alpha(2000) = 18^h06^m49\overset{s}{.}9$, $\delta(2000) = -20°59'57''$, P2 in Table 2), which has a 24 μm source associated with it, P3 to the north (offset 25″), and the maximum (P1) to the south (offset 30″). P2 is near the linewidth maximum (3.3 km s^{-1}), and is also redshifted in centroid velocity. P1, while the strongest in integrated intensity

[5] Since our VLA bandpass included only the central 3.125 MHz of the ∼3.5 MHz hyperfine signature, we observe only the central three of the five main components of the NH_3(1,1) hyperfine signature. To compute the integrated intensity of the line, we assume that the missing outermost lines are 0.22 the strength of the main lines and that the linewidths of all components are equal.

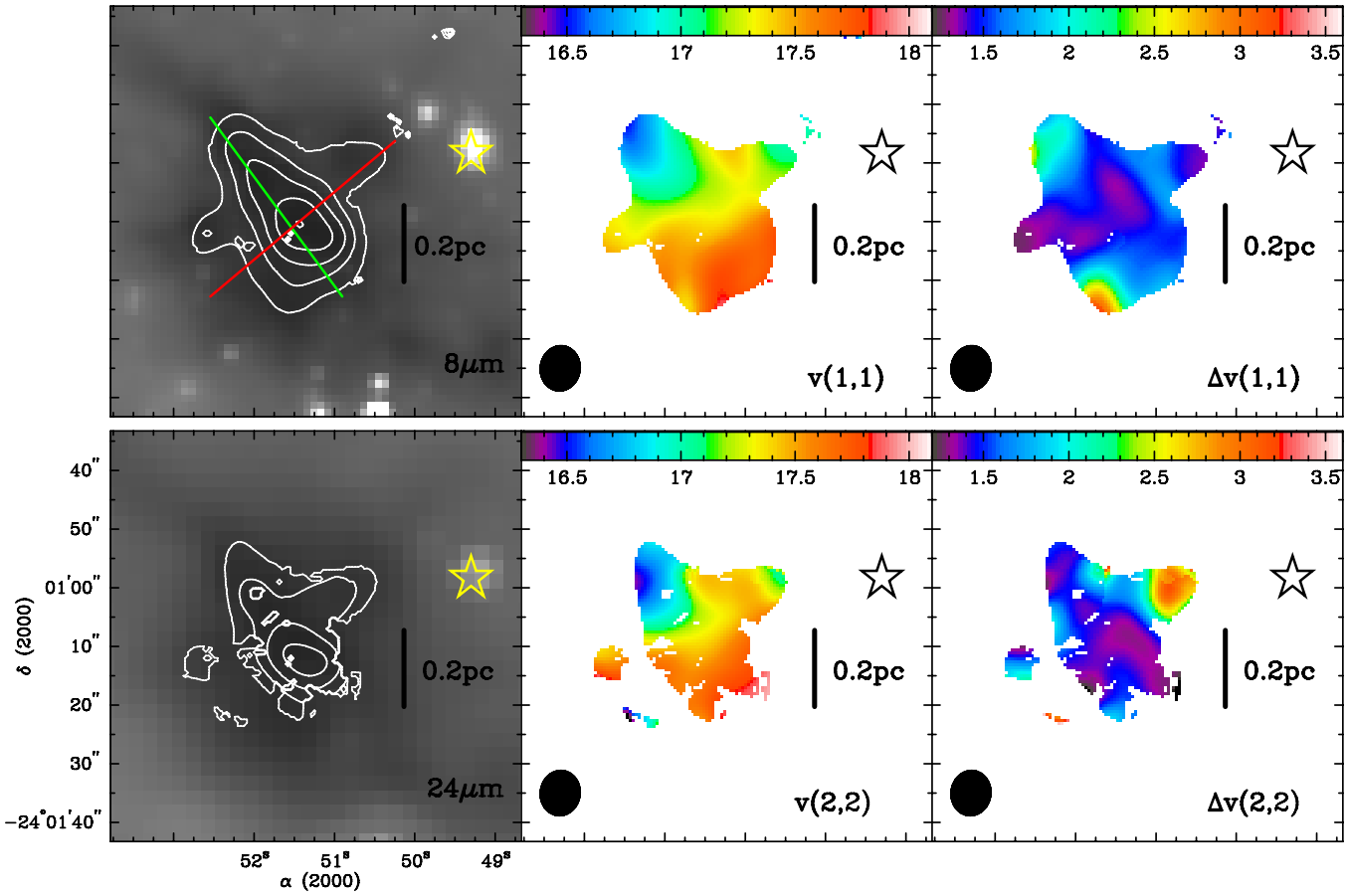

Figure 1. Spectral moments in G005.85−0.23. Top left: *Spitzer*/IRAC 8 μm image with $NH_3(1,1)$ integrated intensity contours overlaid. Contours begin at 0.2 Jy beam^{-1} km s^{-1} and increase in 0.1 Jy beam^{-1} km s^{-1} steps. Bottom left: *Spitzer*/MIPS 24 μm image with $NH_3(2,2)$ integrated intensity contours overlaid. Contours begin at 0.02 Jy beam^{-1} km s^{-1} and increase in 0.01 Jy beam^{-1} km s^{-1} steps. Top center: $NH_3(1,1)$ centroid velocity map in km s^{-1}. Top right: FWHM of $NH_3(1,1)$ central line in km s^{-1}. Bottom center: $NH_3(2,2)$ centroid velocity map in km s^{-1}. Bottom right: FWHM of $NH_3(2,2)$ line in km s^{-1}. The red line represents the major axis and the green line represents the minor axis. The star symbol represents a point source which only appears at 24 μm. The VLA beam is shown at the lower-left corner of the first and second moment panels.

(A color version of this figure is available in the online journal.)

Table 2
Summary of $NH_3(1,1)$ and (2,2) Peak Characteristics

IRDC		Peak $\int T dv$ Position of $NH_3(1,1)$ Transition					$NH_3(2,2)$ Line		R_p	Notes
Name		α (J2000)	δ (J2000)	v_{lsr} (km s^{-1})	Δv (km s^{-1})	$\tau_m(1,1)$	v_{lsr} (km s^{-1})	Δv (km s^{-1})		
G005.85−0.23		17:59:51.4	−24:01:10	17.36 ± 0.02	1.41 ± 0.03	4.9	17.49 ± 0.04	1.37 ± 0.04	0.1	Smooth v-grad.
G009.28−0.15	P1	18:06:50.8	−21:00:25	40.99 ± 0.02	1.45 ± 0.02	4.0	40.99 ± 0.03	1.53 ± 0.03	0.1	Main peak
	P2	18:06:49.9	−20:59:57	41.70 ± 0.07	2.37 ± 0.07	4.0	41.75 ± 0.08	2.14 ± 0.08	0.04	24 μm source
	P3	18:06:49.8	−20:59:34	41.47 ± 0.03	1.85 ± 0.03	3.6	41.38 ± 0.04	1.67 ± 0.05	0.06	24 μm source
G009.86−0.04		18:07:35.1	−20:26:09	17.75 ± 0.04	1.35 ± 0.04	3.3	17.50 ± 0.06	1.64 ± 0.07	0.1	"Quiescent" peak, 2 v-grad.
G023.37−0.29		18:34:54.1	−08:38:21	78.81 ± 0.20	3.89 ± 0.22	... [a]	78.16 ± 0.15	3.66 ± 0.19		24 μm source
G024.05−0.22		18:35:54.4	−07:59:51	81.65 ± 0.03	1.96 ± 0.03	2.6	81.62 ± 0.05	2.14 ± 0.07	0.05	N–S v-grad.
G034.74−0.12	P1	18:55:09.5	+01:33:14	77.95 ± 0.03	2.46 ± 0.03	6.1	77.72 ± 0.05	2.08 ± 0.05	0.04	24 μm source
	P2	18:55:11.0	+01:33:02	78.69 ± 0.03	2.09 ± 0.03	2.9	78.58 ± 0.07	2.04 ± 0.07	0.05	24 μm source

Note. [a] Line saturated.

has the lowest linewidths detected in this object (1.4 km s^{-1}), and there is no associated 24 μm source. The northern integrated intensity peak is 10″ away from a 24 μm point source, but the kinematic structure is not altered by its presence.

Apart from P2 and P3, the bulk of the cloud resides at a narrow range of line-center velocities, between 41 and 41.5 km s^{-1}. The sharpest changes in centroid velocity are located at the eastern edge of the cloud, where the line is blueshifted by 1–1.5 km s^{-1} with respect to the bulk of the cloud at the southeast edge in both $NH_3(1,1)$ and (2,2) emission. The linewidths are also enhanced at this edge, though no young stellar objects (YSOs) are detected in this region.

G009.86−0.04. We approximate this source as a filament, the most elongated structure ($r \sim 2.9$) in our sample. The integrated intensity peak ($\alpha(2000) = 18^h07^m35^s.0$, $\delta(2000) = -20°26'09''$) is dark at both 8 and 24 μm and corresponds to

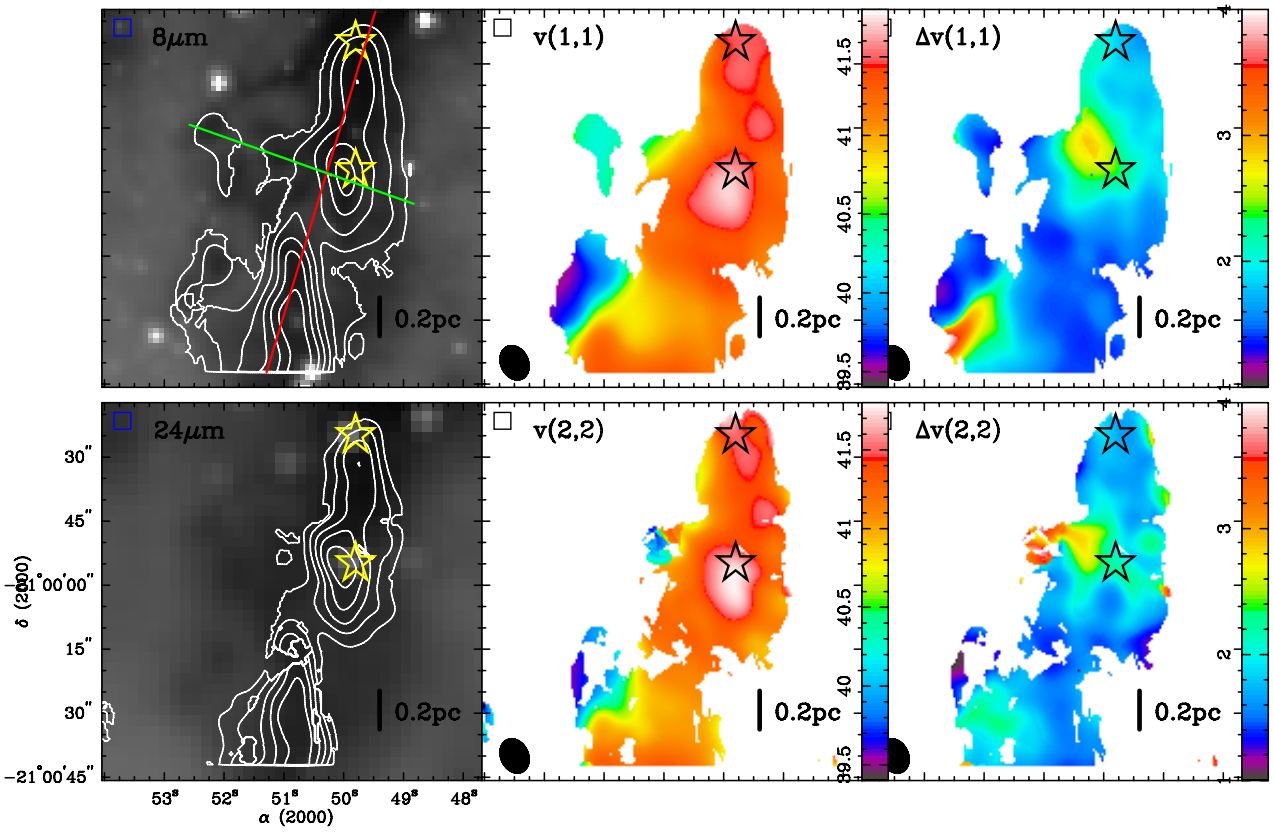

Figure 2. Same as Figure 1 but for G009.28−0.15.
(A color version of this figure is available in the online journal.)

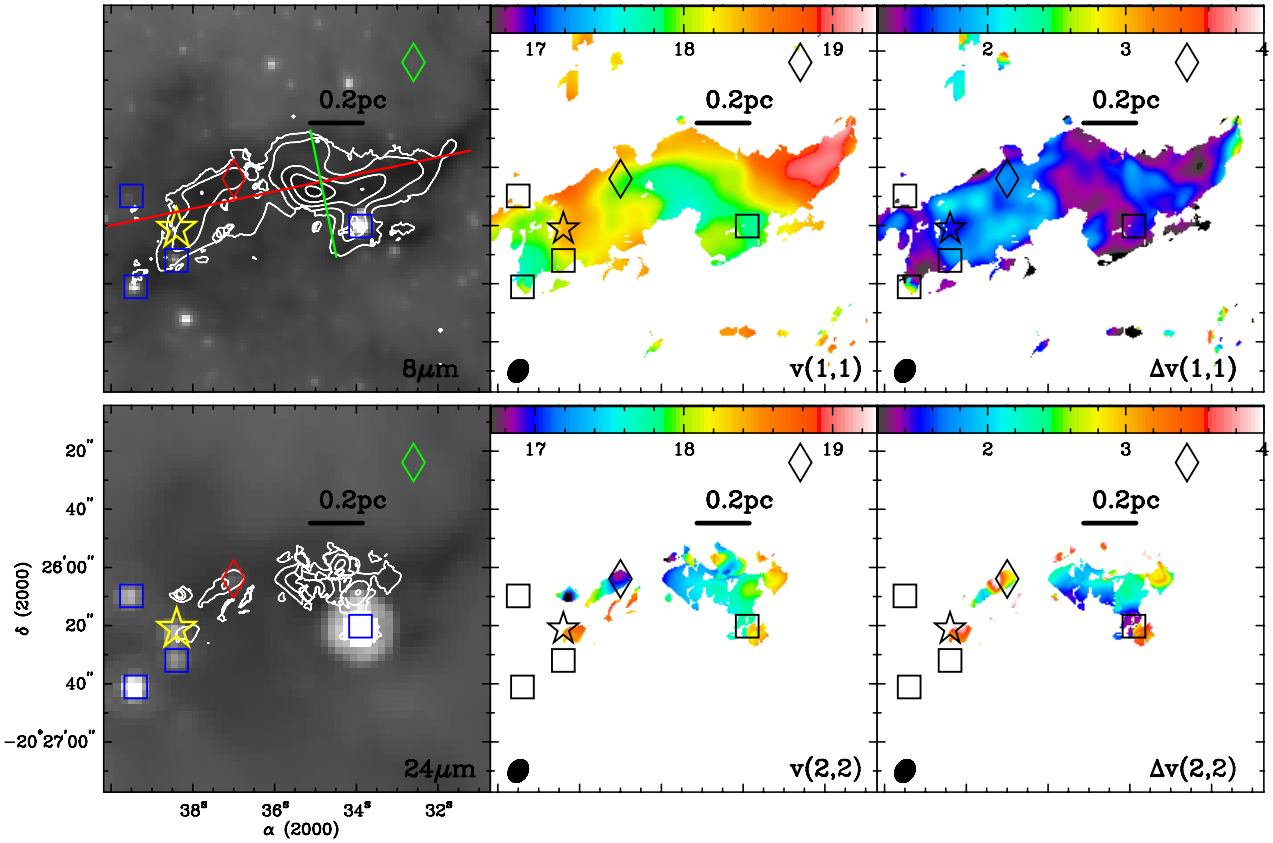

Figure 3. Same as Figure 1 but for G009.86−0.04. $NH_3(2,2)$ integrated intensity contours (overplotted in bottom-left panel) begin at 0.03 Jy beam^{-1} km s^{-1} and increase in 0.01 Jy beam^{-1} km s^{-1} steps.
(A color version of this figure is available in the online journal.)

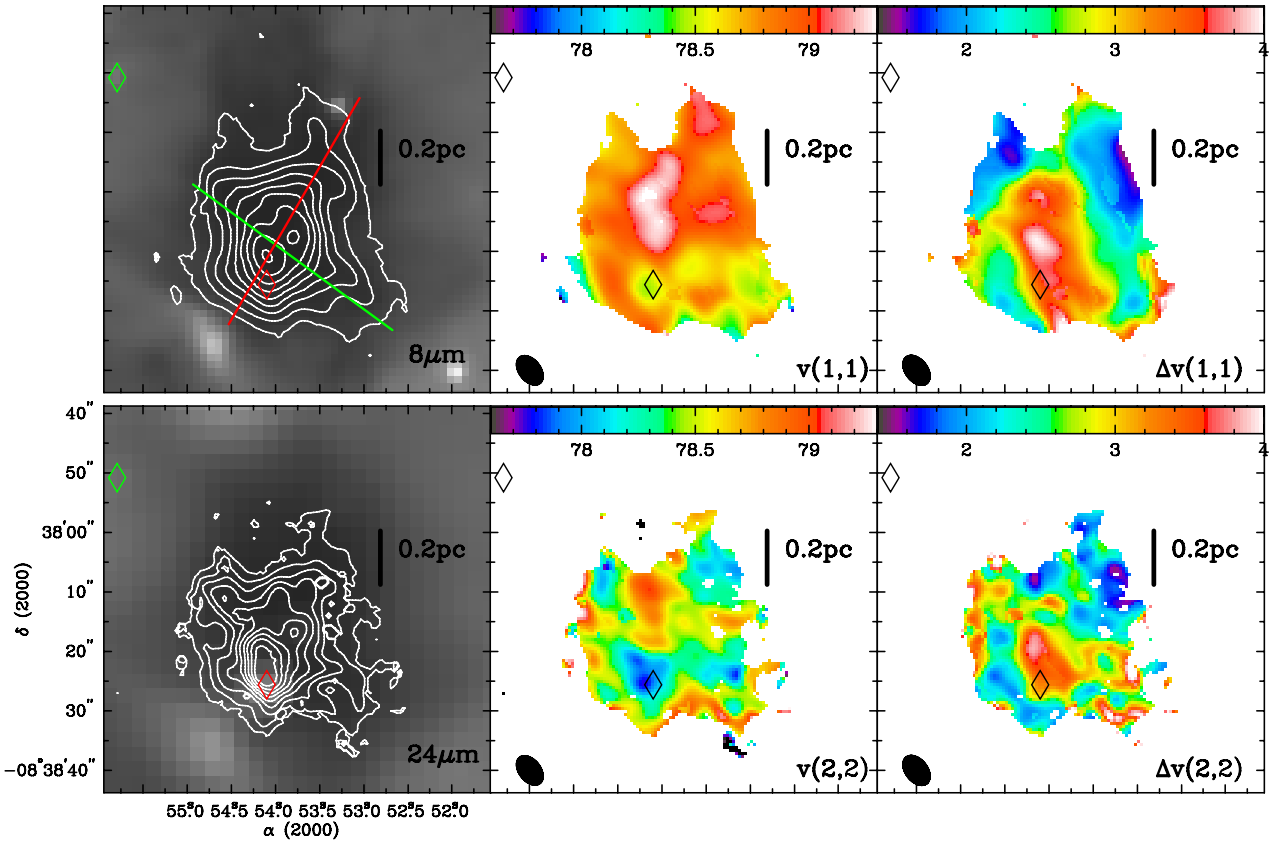

Figure 4. Same as Figure 1 but for G023.37−0.29.
(A color version of this figure is available in the online journal.)

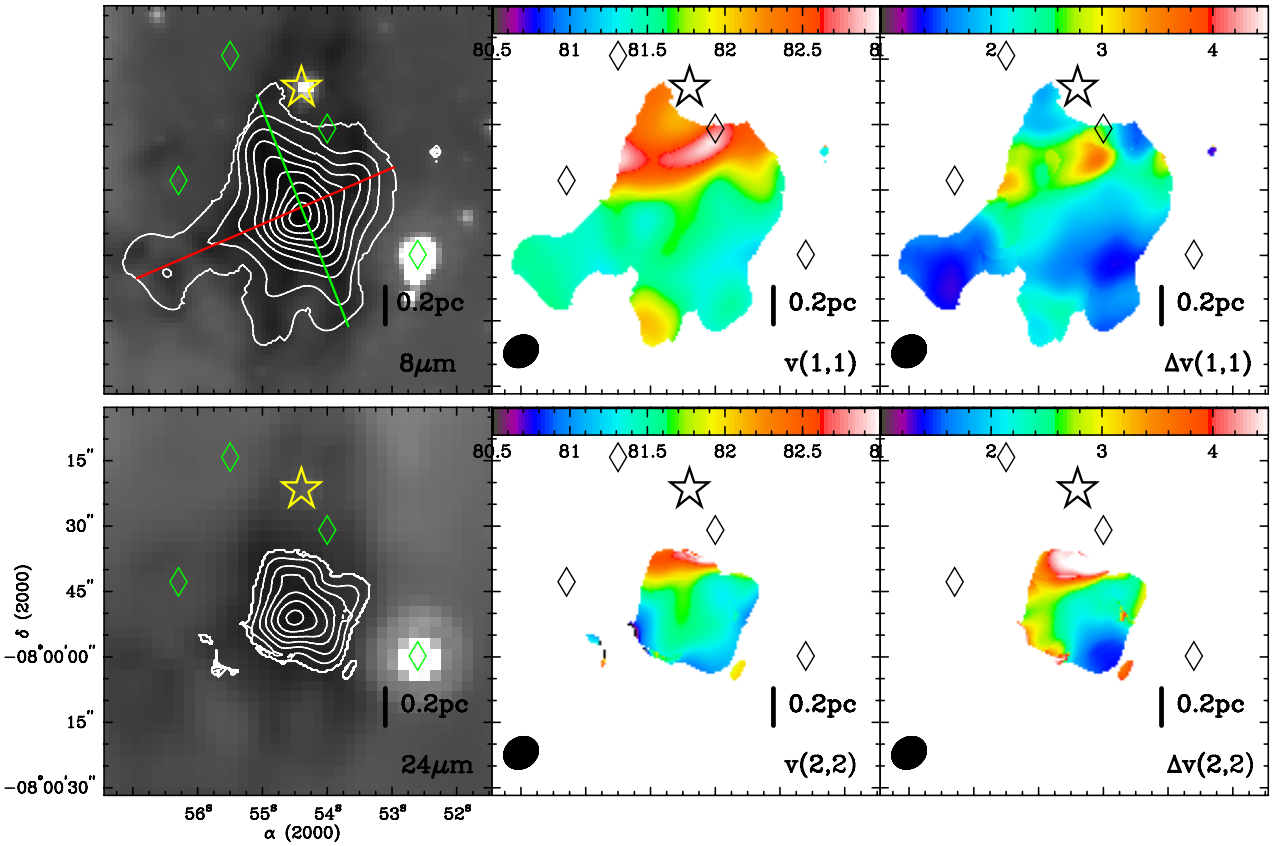

Figure 5. Same as Figure 1 but for G024.05−0.22. $NH_3(2,2)$ integrated intensity contours (overplotted in bottom-left panel) begin at 0.04 Jy beam^{-1} km s^{-1} and increase in 0.01 Jy beam^{-1} km s^{-1} steps.
(A color version of this figure is available in the online journal.)

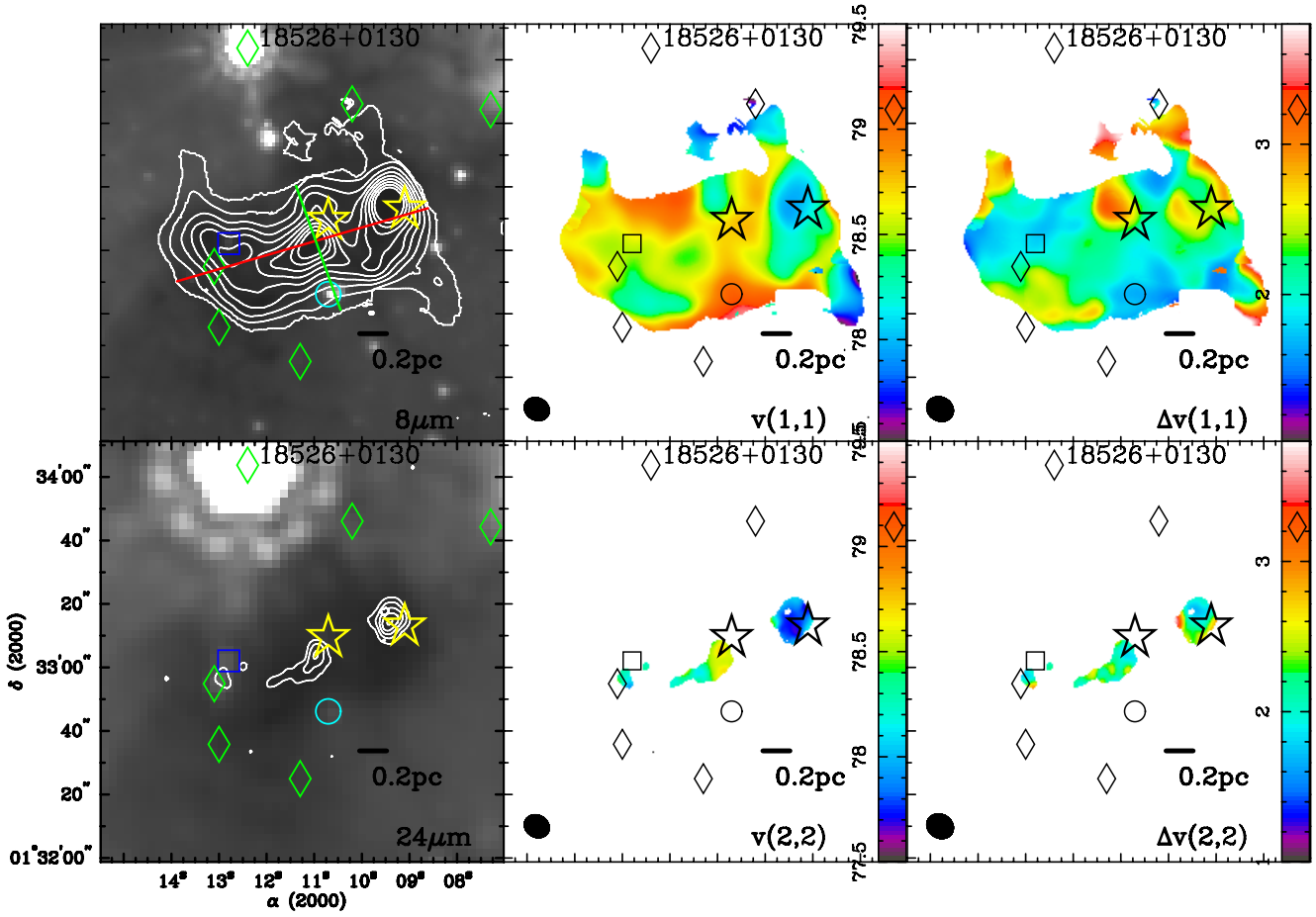

Figure 6. Same as Figure 1 but for G034.74−0.12. NH_3(2,2) integrated intensity contours (overplotted in bottom-left panel) begin at 0.04 Jy beam^{-1} km s^{-1} and increase in 0.01 Jy beam^{-1} km s^{-1} steps.

(A color version of this figure is available in the online journal.)

where the centroid velocity and linewidth are the lowest, all evidence for a quiescent region. The NH_3(1,1) centroid velocity field in this object is organized into two gradients in either direction from the central peak in integrated intensity. The eastern (left-hand) gradient is of magnitude ∼1 km s^{-1} oriented 80° east of north, and the western (right-hand) gradient is of magnitude ∼1.5 km s^{-1} oriented 65° west of north. The central "hinge" position is indistinct in the linewidth measurement.

Overall the velocity field in the filament is smooth, with several YSOs coincident with the ammonia emission: five east of the intensity peak and one to the southwest. The NH_3(1,1) linewidths are enhanced (>2 km s^{-1}) in the east. Curiously, the NH_3(2,2) emission, which appears to follow the locations of the YSOs in the eastern region, exhibits an overall shift to lower line-center velocities (by 0.6 km s^{-1}) and higher linewidths (by 0.5 km s^{-1}). The optical depth of the NH_3(1,1) main line is below ∼3 in the eastern region, so it is unlikely that optical depth effects are the cause of the increased linewidth. This object appears to be undergoing cluster formation, though the part of the cloud associated with NH_3(1,1) emission peak remains quiescent.

G023.37−0.29. The integrated intensity map of this round IRDC ($r \sim 1.1$) peaks at $\alpha(2000) = 18^h34^m54\overset{s}{.}1$, $\delta(2000) = -8°38'21''$, although throughout this cloud, the lines are saturated and/or optically thick, making it impossible to derive reliable optical depths or very accurate line properties. There is a 24 μm point source (not present at 8 μm) near the center of the region, slightly offset from the intensity peak, which is likely a deeply embedded protostar. The central region has very high linewidths (highest in the sample, 4 km s^{-1}, see Figure 4), although because of the high optical depth of the NH_3 lines, these should be taken cautiously.

G024.05−0.22. This approximately round source ($r \sim 1.1$) appears centrally peaked in line intensity (left panels of Figure 5) at $\alpha(2000) = 18^h35^m54\overset{s}{.}1$, $\delta(2000) = -7°59'51''$, which corresponds also to the peak in 8 μm optical depth. The NH_3(1,1) map shows a velocity gradient starting at an east–west aligned "ridge" slightly offset to the north from the peak of integrated intensity. This "ridge" in centroid velocity also corresponds with enhanced linewidths (∼3.6 km s^{-1}) in both the (1,1) and (2,2) lines, though with no distinction in integrated intensity similar to what we see in G009.86−0.04. From the center of the cloud across this ridge, the velocity changes by ∼1.1 km s^{-1}, and corresponds to a gradient of 2.1 km s^{-1} pc^{-1}. At the southern tip of (1,1) emission, there appears to be a clump with distinct redshifted velocity but this is not detected in (2,2) emission. While there is one Class II source coincident with northern ridge, this IRDC lacks 24 μm detections (an indicator of an embedded source) anywhere in the cloud.

G034.74−0.12. The overall velocity field of this filament ($r \sim 2.0$) appears quite disorganized, particularly in locations where 24 μm point sources are detected. There are two integrated intensity peaks in this IRDC, both in the vicinity of 24 μm sources (star symbols in Figure 6), and both positions show high linewidth. The strong NH_3(1,1) peak in the northwest portion

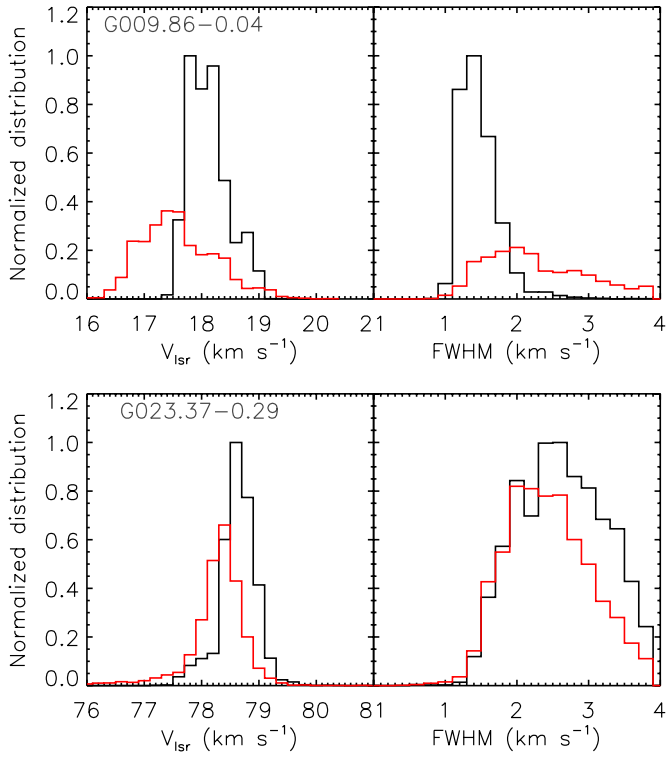

Figure 7. Distribution of velocity fit parameters for IRDC G009.86−0.04 and G023.37−0.29 with the NH_3(1,1) plotted in the black histogram and the NH_3(2,2) distribution plotted in the red histogram. Both histograms are normalized to the number of positions with a (1,1) measurement. The left panel shows the line-center velocities and the bottom panel shows the FWHM, both in km s^{-1}.

(A color version of this figure is available in the online journal.)

of the cloud (α(2000) = $18^h55^m09\overset{s}{.}5$, δ(2000) = +1°33′14″, P1 in Table 2) is directly coincident with a 24 μm point source, enhanced linewidths and a slightly blueshifted centroid velocity. The optical depth of the NH_3(1,1) main line is 6.1. The centrally located peak (α(2000) = $18^h55^m11\overset{s}{.}0$, δ(2000) = +1°33′02″, P2 in Table 2) is offset 10″ from the position of the 24 μm source and offset 15″ from the nearby peak in linewidth. The optical depth of the NH_3(1,1) line here is 2.9. These two locations are also where most of the appreciable NH_3(2,2) emission is found.

3.2. Comparison between (1,1) and (2,2) Kinematics

As is shown in the left panels of Figures 1–6 the NH_3(1,1) emission tends to be more widespread than the (2,2) emission. In this section, we compare the velocity fields of the two states. The central panels show the range in line-center velocities, which generally encompass the same range, and the right panels show similar trends in linewidth. Table 2 shows the velocity properties of the (1,1) and (2,2) at the locations of the NH_3(1,1) intensity peaks.

In G009.86−0.04 and, to a lesser extent in G023.37−0.29, we find that the median NH_3(2,2) line-center velocity is offset to lower velocities by ∼0.6 km s^{-1} compared to the NH_3(1,1), and the median FWHM of the (2,2) line is higher than that of the (1,1) line by ∼0.8 km s^{-1}. Figure 7 shows the distributions of line-center velocity and linewidth from both the (1,1) and (2,2) maps. G009.86−0.04 has several young stars and 24 μm point sources in the eastern part of the cloud, which corresponds to the locations of the high linewidths and blueshifted line-center velocities in the NH_3(2,2) map. The optical depth of

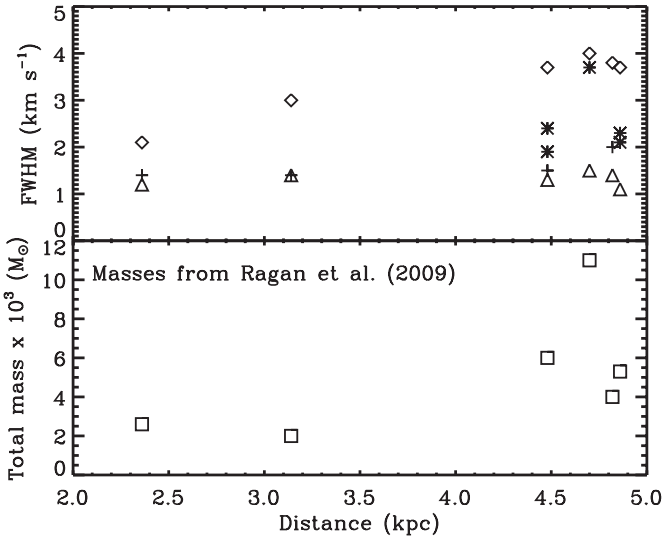

Figure 8. Top: linewidth vs. IRDC distance. The linewidth at the integrated intensity peaks (marked with asterisks where there 24 μm point sources present and + signs for those without 24 μm point sources) and the maximum detected linewidth overall in the cloud (marked with diamonds) both increase with increasing distance. Bottom: total mass (from 8 μm absorption; Ragan et al. 2009) vs. distance.

the NH_3(1,1) main line is less than 3 in this region, lower than typical values of 4 or 5 throughout the sample, so it is unlikely that optical depth effects are the cause of the enhanced linewidth. It may be the case that the young stars are having a dynamical effect on the slightly warmer gas probed by the NH_3(2,2) emission. This does not appear to be the case in G023.37−0.29, where there is only a singular 24 μm point source and the lines are optically thick, which would likely limit our ability to probe near any embedded source(s).

IRDC G034.74−0.12 also exhibits evidence that a cluster is actively forming with the two 24 μm point sources corresponding to very strong NH_3 emission and several other young stars in the vicinity. However, in these two locations of 24 μm point sources, which is also where most of the NH_3(2,2) emission is detected, the linewidth appears more enhanced in the NH_3(1,1) rather than (2,2). We note that the high optical depth of NH_3(1,1) at P1 (6.1) may contribute to the broadened line here. The observations of this object were the noisiest of the sample, and it is also the most distant IRDC, so we may not be sensitive to the effect we see in G009.86−0.04 (the nearest IRDC).

3.3. Linewidth

The NH_3(1,1) linewidths in our sample of IRDCs are between 1.1 and 4 km s^{-1}, occupying the high tail of the linewidth distribution presented in the Jijina et al. (1999) survey of 264 dense cores, but on par with other ammonia studies of IRDCs: Pillai et al. (2006), who found a slightly lower range in their single-dish study, and Wang et al. (2008), who found that different cores within an IRDC exhibited different linewidths in the high-resolution study: higher linewidths near locations of embedded star formation activity and lower linewidths in quiescent regions of the cloud. For our sources, the enhanced linewidth appears to correspond to the locations of 24 μm point sources.

We find that the linewidth increases with increasing distance to IRDCs, as was noted by Pillai et al. (2006). In Figure 8, we show that the maximum linewidth detected in IRDCs varies directly with distance, which may be a result of clumping within

the beam increasing with distance. Certainly, with *Spitzer* we do see objects on the 2″–3″ scale which would not be resolved with the beam (sometimes 6″–8″ in low-elevation sources). At the same time, the minimum linewidth does not show any trend with distance. As noted above, the integrated intensity peaks with 24 μm point sources have a higher linewidth than those peaks without, but the apparently starless peaks typically have very low linewidths, independent of distance ($\Delta v \sim 1.4\,\mathrm{km\,s^{-1}}$). Therefore, in the following discussion, we proceed with our analysis assuming that the trends are intrinsic features not determined by the distance. As shown in the lower panel of Figure 8, the cloud masses increase slightly with distance, which could simply be a selection effect. Higher cloud masses suggest deeper gravitational potentials, which in turn would give rise to larger linewidths. Yet the total kinetic energy calculated from the averaged linewidths and the centroid velocities does not change perceptibly with distance.

The dynamical properties of all IRDCs are summarized in Figure 9. The centroid velocity distributions (left column) are asymmetric, with tails to lower or higher velocities than the systemic velocity. This could indicate a substantial elongation along the line of sight, or highly asymmetric infall. The relative motions to the systemic velocity are mostly supersonic. The non-thermal velocity dispersion

$$\sigma_{\mathrm{NT}} = \sqrt{\frac{\Delta v^2}{8\ln 2} - \frac{k_B T}{\mu m_H}} \quad (1)$$

is larger than the sound speed (see Paper I for temperatures, ranging from 8 to 13 K) for all IRDCs—in fact, none of the velocity dispersions are smaller than Mach 2. The distributions are peaked, with tails to high Mach numbers. For IRDCs containing sources (see discussion above), these tails, or "excesses" are correlated with locations in the vicinity of the sources.

4. DISCUSSION

Judging from Figures 1 through 6, it is unlikely that one model of IRDC kinematics can fully account for the range of behaviors observed. The broad characteristics—the overall linewidths and ranges of centroid velocities, see Table 2—are roughly consistent among the clouds in the sample and with previous molecular line studies (e.g., Pillai et al. 2006; Ragan et al. 2006). However, our sample exhibits both global trends (e.g., smooth velocity gradients) and localized effects (e.g., signatures of feedback from young embedded protostars) that can now be investigated with high angular resolution observations.

As a first approximation of stability, we compute the virial mass of the clouds ($M_{\mathrm{Virial}} = 5RV_{\mathrm{rms}}^2/(3G)$), where R is the radius of the cloud, G is the gravitational constant, and $V_{\mathrm{rms}} = 3^{1/2}\Delta V/2.35$ where ΔV is the average linewidth of the cloud. Virial masses for the whole clouds are typically $10^{2-3}\,M_\odot$, and the virial parameters, $\alpha = M_{\mathrm{Virial}}/M$, from 0.1 to 0.7, suggesting that IRDCs are bound structures prone to collapse. The cloud masses M are taken from the dust extinction maps by Ragan et al. (2009).

The linewidths observed in our sample (1.1–4.0 km s^{-1}) are in excess of the thermal linewidth, ~0.18 km s^{-1}. The ratio of thermal to non-thermal pressure in the cloud, as expressed by Lada et al. (2003), is $R_p \equiv c_s^2/\sigma_{\mathrm{NT}}^2$, where c_s is the isothermal sound speed and σ_{NT} is the three-dimensional non-thermal velocity dispersion. We calculate values for R_p at each of the intensity peaks in the IRDCs (see Table 2) and find an average value of 0.07, indicating that non-thermal pressure is dominant. "Non-thermal effects" encompass many things, such as infall, outflows, or systematic cloud motions (i.e., rotation) and possible "support" from turbulent motions (Arons & Max 1975) or magnetic fields (Mouschovias & Spitzer 1976). In the following sections, we explore these effects individually, so to determine the dominant processes.

4.1. Connecting Star Formation and IRDC Kinematics

The IRDCs in our sample span a range of stages of star formation, some devoid of embedded sources and some hosting several. In Paper 1, we showed that the presence of young stars does not significantly affect the kinetic temperature of the gas traced by ammonia, at least beyond the ~1 K errors we estimate.[6] However, as we showed in Section 3.1, the presence of young stars, particularly 24 μm point sources, has a localized effect on the IRDC dynamics, namely, an increase in linewidth at the positions of young stars and (sometimes) distinct centroid velocity components. We see no strong trend for the positions of the 24 μm point sources to have exceptionally high optical depths in NH_3(1,1), thus we do not expect optical depth effects to contribute strongly to linewidth enhancements. Furthermore, starless peaks in NH_3 intensity (existing in all clouds except G023.37−0.29 and G034.74−0.12) tend to have the lowest linewidths.

Broadened linewidths are an indicator of increased internal motions which accompany the onset of star formation (Beuther et al. 2005). In each IRDC (except G005.85−0.23 and G024.05−0.22) of our sample, we see that the sites of 24 μm point sources are accompanied by an enhancement in NH_3(1,1) linewidth (in G009.86−0.04, the enhancement is rather seen in the NH_3(2,2) linewidth). Beuther et al. (2005) found that in a molecular core with an infrared counterpart, the N_2H^+(1–0) emission (known to trace dense gas similarly to NH_3, e.g., Johnstone et al. 2010) exhibited broad line emission, whereas linewidths in infrared-dark cores—presumably at an earlier evolutionary stage—were significantly narrower ($\Delta v \sim 1$ km s^{-1}). The increased internal motions giving rise to broadened lines can be attributed to ordered motion, such as infall, outflow, or rotation.

4.2. Kinematics of "Starless" IRDCs

Because the feedback from embedded protostars can confuse the kinematic signatures in the IRDCs, here we take a closer look at the IRDCs which show little or no evidence of actively forming stars. Our sample includes one IRDC, G005.85−0.23, which lacks any coincident *Spitzer* point sources, thus does not appear to host embedded star formation. G024.05−0.22 has one Class II object (with no 24 μm counterpart, see Figure 5) near the edge of the NH_3(1,1) emitting region, thus the bulk of the IRDC appears devoid of YSOs. It is possible in both cases that embedded protostars in the IRDC are heavily extincted by dust beyond our detection limit, but we continue our discussion assuming that the kinematics are dominated by the global forces rather than protostellar feedback.

Both of these IRDCs have nearly round projected morphologies. In G005.85−0.23, the gradient is from southwest to northeast (33° east of north) centered on the integrated intensity peak.

[6] We noted in Paper 1 that these observations of the (1,1) and (2,2) transitions of ammonia are not necessarily sensitive to hotter gas on the smallest scales, which (for example) may arise from a young embedded protostar heating a compact core. Gas in warm, compact regions are better probed with higher-J transitions of ammonia or other molecules.

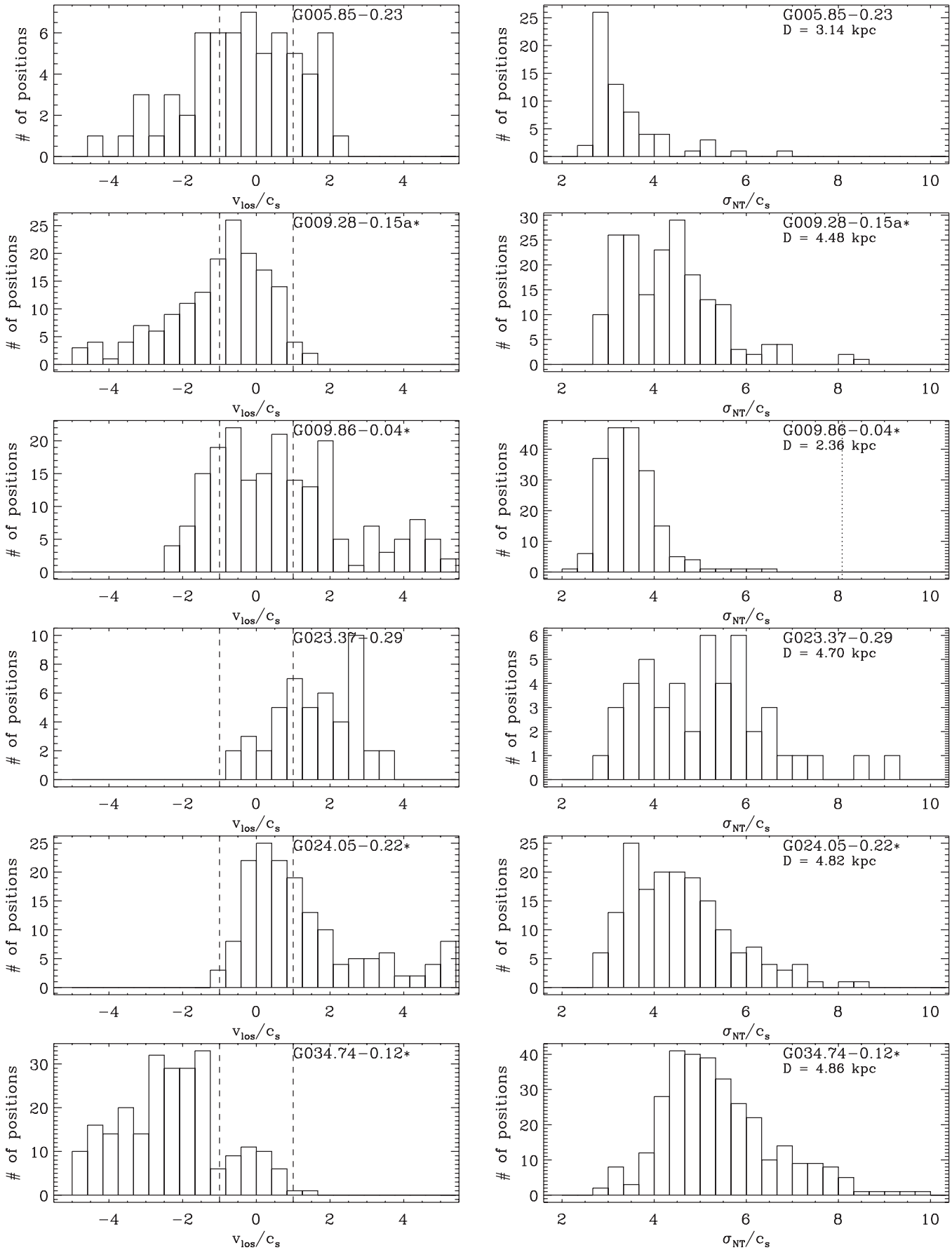

Figure 9. Summary of IRDC kinematics. Left column: histograms of the centroid velocity in units of the sound speed. Vertical dashed lines indicate the transition between subsonic and supersonic. Right column: histograms of the non-thermal velocity dispersion (Equation (1)). All values are supersonic by at least a factor of two.

In G024.05−0.22 the gradient is from northeast to southwest (8° east or north) but is not symmetric about the peak in integrated intensity. In this case, the velocity gradient is not smooth, but has a sharp ridge structure in the east–west direction, which also corresponds with enhanced linewidths (∼3.6 km s^{-1} compared to <2 km s^{-1} throughout the rest of the cloud).

Smooth velocity gradients are often interpreted as signatures or rotation (e.g., Arquilla & Goldsmith 1986; Goodman et al. 1993). Since the projected geometry of both of these IRDCs is roughly circular, we can reasonably approximate the clouds as spheres. If we assume solid-body rotation, the resulting velocity gradients are 2.4 and 2.1 km s^{-1} pc^{-1} for G005.85−0.23 and G024.05−0.22, respectively. If this organized motion is linearly fit and subtracted from the centroid velocity field, the residuals are less than 0.2 km s^{-1}.

We can then compare the importance of rotational kinetic energy to gravitational energy, parameterized by the ratio, β (in this case for a uniform density sphere), defined as $\beta = \Omega^2 R^3/(3GM)$, where Ω is the angular velocity, R is the cloud radius, and M is the cloud mass (Goodman et al. 1993). For the mass, we take values from Ragan et al. (2009) using 8 μm absorption as a mass-tracer over the region mapped in ammonia. For reference, a value of $\beta = 1/3$ is equivalent to breakup speed for a spherical cloud, and lower values signify a lessening role of rotation in cloud energetics. Under these assumptions, we find β values of 2×10^{-4} and 5×10^{-4}, lower than the extremely low end of the β range seen in dark cores (Goodman et al. 1993) because the masses are much higher (500 and 2500 $M_\odot$, respectively). Adopting a more realistic centrally peaked density profile, $\rho \propto r^{-2}$ for example, reduces β by a factor of three. In this simplistic picture, rotation plays only a small role in the dynamics of the cloud.

Such a simple solid-body rotation model for such spherical IRDCs is a tempting interpretation, but one that should be made cautiously. Burkert & Bodenheimer (2000) show that large-scale turbulent motions (i.e., turbulence with a steep power spectrum) can lead to centroid velocity gradients that look like shear or rotation. Indeed, even in these IRDCs which appear to be the most quiescent, the linewidths far exceed the thermal sound speed in the typical IRDC environment (about 0.2 km s^{-1}). Such linewidths could be caused by outflows from a low-mass stellar component not detectable in the Ragan et al. (2009) *Spitzer* observations. Even in the absence of stellar feedback, non-thermal linewidths would be expected as consequence of the cloud formation (e.g., Vázquez-Semadeni et al. 2007; Heitsch et al. 2008b), or if global gravitational collapse dominates the cloud evolution (e.g., Burkert & Hartmann 2004; Field et al. 2008). Below, we examine these possibilities in greater detail.

4.3. Dynamical Conditions of IRDCs

To refine our energetics estimates of the previous section, we analyzed the spatial energy distribution within the clouds. To date, dynamical studies of IRDCs have been limited mainly to single-dish surveys with resolution elements of ∼30″, which is insufficient to resolve the relevant (sub-parsec) scales. With our VLA data set, we have mapped the velocity field across an IRDCs, so we are now able to quantify the energy distribution in IRDCs. To determine the degree of stability, we will fit (idealized) geometries, guided by our classification of the IRDCs in "spheres" and "filaments" (see Table 3). The fits result in density profiles, isothermal temperatures, and a criticality parameter (see below). We use the fitted temperatures as a measure of the energy required to balance gravitational and kinetic energy content, which can be compared to the measured temperatures from Paper I. The fit results are summarized in Table 3.

Table 3
Summary of Fit Results

IRDC Name	Geometry[a]	n_0[b] (cm^{-3})	T_0[c] (K)	ξ_n[d]	σ_{res}[e] (km s^{-1})	Δ[f]
G005.85−0.23	Sphere	1.1×10^6	5.0×10^3	1.1	2.4	0.18
G009.28−0.15a	Filament	4.0×10^5	5.4×10^3	2.3	2.5	0.23
G009.28−0.15b	Filament	8.9×10^5	1.2×10^4	5.5	3.8	0.27
G009.86−0.04	Filament	6.8×10^5	2.0×10^3	6.2	1.6	0.28
G023.37−0.29	Sphere	6.0×10^5	6.0×10^3	1.7	2.6	0.31
G024.05−0.22	Sphere	5.5×10^5	6.0×10^3	1.7	2.7	0.4
G034.74−0.12	Filament	3.4×10^5	2.3×10^4	2.0	5.3	0.18

Notes.
[a] Fitting geometry (BE-sphere or isothermal cylinder).
[b] Fitted central density.
[c] Fitted isothermal temperature.
[d] Normalized stability parameter. $\xi_n = \xi_{ml}$ for cylinders and $\xi_n = \xi_{BE}/6.5$ for BE-spheres. $\xi_n > 1$ indicates instability.
[e] Residual velocity dispersion needed at minimum to support the cloud energetically.
[f] Normalized rms error of fit.

4.3.1. "Filaments"

For the filament-like clouds, we construct radial mass density profiles from the dust column densities assuming an isothermal cylinder as the underlying model. The density profile for an isothermal cylinder is given by

$$\rho(r) = \frac{\rho_0}{(1 + (r/H)^2)^2}, \quad (2)$$

with the cylinder scale height

$$H^2 \equiv \frac{2c_s^2}{\pi G \rho_0} \quad (3)$$

(e.g., Ostriker 1964), with the sound speed $c_s \equiv \sqrt{k_B T_0/(\mu m_H)}$. The fitting is done in two steps. First, we construct a filament following the mass distribution as traced by dust extinction with *Spitzer* (Ragan et al. 2009) by calculating the center-of-mass positions along the R.A. and decl. axes. A linear regression through the resulting positions results in the filament axis, from which the distances of the sample positions are calculated. This gives us a radial column density profile $N_{obs}(r)$. Next, for the fitting, we start with an initial guess of ρ_0, T_0, and R_0, construct a profile using Equation (2) and project it to generate a column density profile $N_{cyl}(r)$. The rms difference

$$\Delta_{rms} = \sum_i (N_{obs}(r_i) - N_{cyl}(r_i))^2 \quad (4)$$

between the data and this profile is then minimized by a downhill simplex method in the three parameters ρ_0, T_0, and R_0. For each cloud, we check a map of Δ_{rms} to ensure that the fit does not converge on a local minimum (it never did).

To estimate the degree of stability, we compare the fitted temperature, T_0, which range between 2.0×10^3 and 2.3×10^4 K, to the cloud temperatures presented in Paper I—typically between 8 and 13 K. We convert the difference in temperatures to a "residual velocity dispersion" (σ_{res}) that would be needed

to support the cloud against collapse, from 1.6 to 5.3 km s^{-1}. These parameters are summarized in Table 3. We also take the ratio of the mass per unit length derived from the fit over the corresponding critical value (Ostriker 1964),

$$\xi_{\rm ml} \equiv \frac{m}{m_c} = \frac{\pi G R_0^2 \rho_0}{2c_s^2} \frac{16H^2}{16H^2 + R_0^2}, \quad (5)$$

with a mean molecular weight of $\mu = 2.36$. Note that the fitted temperature T_0 is *not* the temperature needed to stabilize the filament against collapse, since we fit all three parameters, central density, temperature, and radius. Thus, for $\xi_{\rm ml} > 1$, the filament will collapse.

Figure 10 summarizes the results. The left column shows the dust column profiles (symbols) and the best fit (solid line) with the corresponding parameters. As is already suggested by the maps, there is a substantial scatter in the profiles, resulting in relative rms errors between 20% and 30%. Note that we split up G009.28−0.15 into two components divided at $\delta = -21^\circ00'20''$, just as was done in Paper I. The non-thermal velocity dispersion profiles (Equation (1)) are given in the right column, with the data shown in symbols, a linear regression in a dashed line, and a binned version in the solid line (including error bars). The dot-dashed line indicates the residual velocity dispersion that would be (at minimum) required for cloud turbulent support given the nominal fit temperature and the (observed) actual temperature.

All "filaments" are gravitationally unstable by at least a factor of two in terms of masses, consistent with the virial estimates made above. The non-thermal velocity dispersions $\sigma_{\rm NT}$, typically between 0.5 and 2 km s^{-1} (corresponding to hundreds of Kelvin), are at least a factor of two below the formally required value for support, $\sigma_{\rm res}$. If $\sigma_{\rm NT}$ were to give rise to an isotropic pressure as envisaged in models of turbulent support (McKee & Tan 2002, 2003), then its gradient is inconsistent with such a scenario for at least two IRDCs (G023.37−0.29 and G009.28−0.15b). The remaining IRDCs show strong scatter in the velocity profiles, indicating that there is no systematic velocity distribution.

4.3.2. "Spheres"

IRDCs with roughly circular shapes (or at least not obviously filamentary ones) we approximate by a (projected) Bonnor–Ebert sphere. The same reasoning as in Section 4.3.1 applies, namely, that we are interested in the nominal temperature required to provide pressure support against collapse. We solve the modified Lane–Emden equation (Ebert 1955; Bonnor 1956)

$$\frac{d}{d\xi}\left(\xi^2 \frac{d\psi}{d\xi}\right) = \xi^2 e^{-\psi} \quad (6)$$

$$\xi \equiv \frac{R}{c_s}\sqrt{4\pi G n_0 \mu m_H}, \quad (7)$$

integrating the ordinary differential equations with a fourth-order Runge–Kutta scheme, with initial conditions $\psi(0) = 0$ and $d\psi(0)/d\xi = 0$. A solution is determined by the central core density n_0, the isothermal temperature T_0, and the radius $R_{\rm max}$. For $R > R_{\rm max}$, the density is assumed to drop to irrelevant values, with the temperature increasing to provide pressure equilibrium at $R_{\rm max}$. For values of $n_0/n(R_{\rm max}) > 14.3$, or $\xi_{\rm BE} > 6.5$, the BE-sphere is gravitationally unstable and will collapse.

In a procedure similar to the filament fitting, we construct radial column density profiles from the dust data, which we then fit with a two-dimensional projection of a BE-sphere. We chose to fit all three parameters, n_0, T_0, and $R_{\rm max}$, instead of constraining the fits by the observed cloud radius $R_{\rm obs}$ and the central column density, because having the BE-sphere extend to $R_{\rm max} = R_{\rm obs}$ results in compact column density profiles, i.e., the column density would drop to zero at $R_{\rm obs}$, inconsistent with the shape of the observed column density profiles. Thus (again), the resulting BE temperatures are *not* the temperatures needed to support the sphere, but they are generally smaller.

Figure 11 summarizes the results analogously to Figure 10. We show the radial column density profiles, the best fit and its parameters, and the velocity profiles with a linear regression, a binned profile, and the turbulent residual velocity needed to support the cloud. Comparing this to the actual dispersions gives us a measure of cloud stability. Again the fitted temperatures are on the order of 5–6 $\times$ 10^3 K.

All fits result in unstable BE-spheres. The $\xi_{\rm BE}$-values are super-critical even at the nominal (fitted) temperatures which are more than two orders of magnitude larger than the observed temperatures. The $\sigma_{\rm NT}$-profiles are more than a factor of two below the dispersion required for support, and the observed values show again a substantial scatter, indicating a strong degree of anisotropy in the spatial kinetic energy distribution.

4.3.3. Implications of Fitting Results

The above discussion leads us to conclude the following. All IRDCs in our sample are gravitationally unstable, with $\xi_{\rm ml} > 1$, $\xi_{\rm BE} > 6.5$ (see Table 3). The fitted temperatures are at least two orders of magnitude higher than the observed values for all IRDCs, yet the fits still result in unstable structures. Interpreting these temperatures as "turbulent temperatures," the kinetic energy (including systematic motions as indicated by the centroid velocity) in the clouds is insufficient to provide support against collapse, consistent with our earlier virial estimates. The scatter of the velocity profiles is substantial (in cases more than 100%), suggesting that local gravitational motions dominate over "micro-turbulent" motions. The latter have been repeatedly demonstrated to be inconsistent with observational and numerical evidence (e.g., Brunt & Heyer 2002; Padoan et al. 2003; Brunt et al. 2009).

Another way to view our results is to consider the "turbulent residual velocity dispersion" (dot-dashed line in Figures 10 and 11) as a measure for the *gravitational* energy within the IRDC. Then, its ratio to the observed dispersion values of a few is consistent with the ratios between gravitational and kinetic energies found in models of collapsing molecular clouds (Vázquez-Semadeni et al. 2007; Heitsch et al. 2008a), in which the non-thermal ("turbulent") linewidths in molecular clouds are driven by global gravitational collapse, with the kinetic energy trailing the gravitational energy by a factor of a few (see Figure 8 of Vázquez-Semadeni et al. 2007 and Figure 10 of Heitsch et al. 2008a).

Expanding on this thought, Figure 12 shows centroid velocity histograms taken along three lines of sight from a model of flow-driven cloud formation (model Gf2 of Heitsch et al. 2008a). The centroid velocities were measured at a point when the cloud is gravitationally collapsing, and forming local gravitationally bound cores. The selected lines of sight are centered on three of the most massive cores in the Heitsch et al. study (numbers 2, 5, and 8). The clouds form due to the collision of two warm, diffuse gas flows. Strong hydrodynamical and thermal instabilities lead

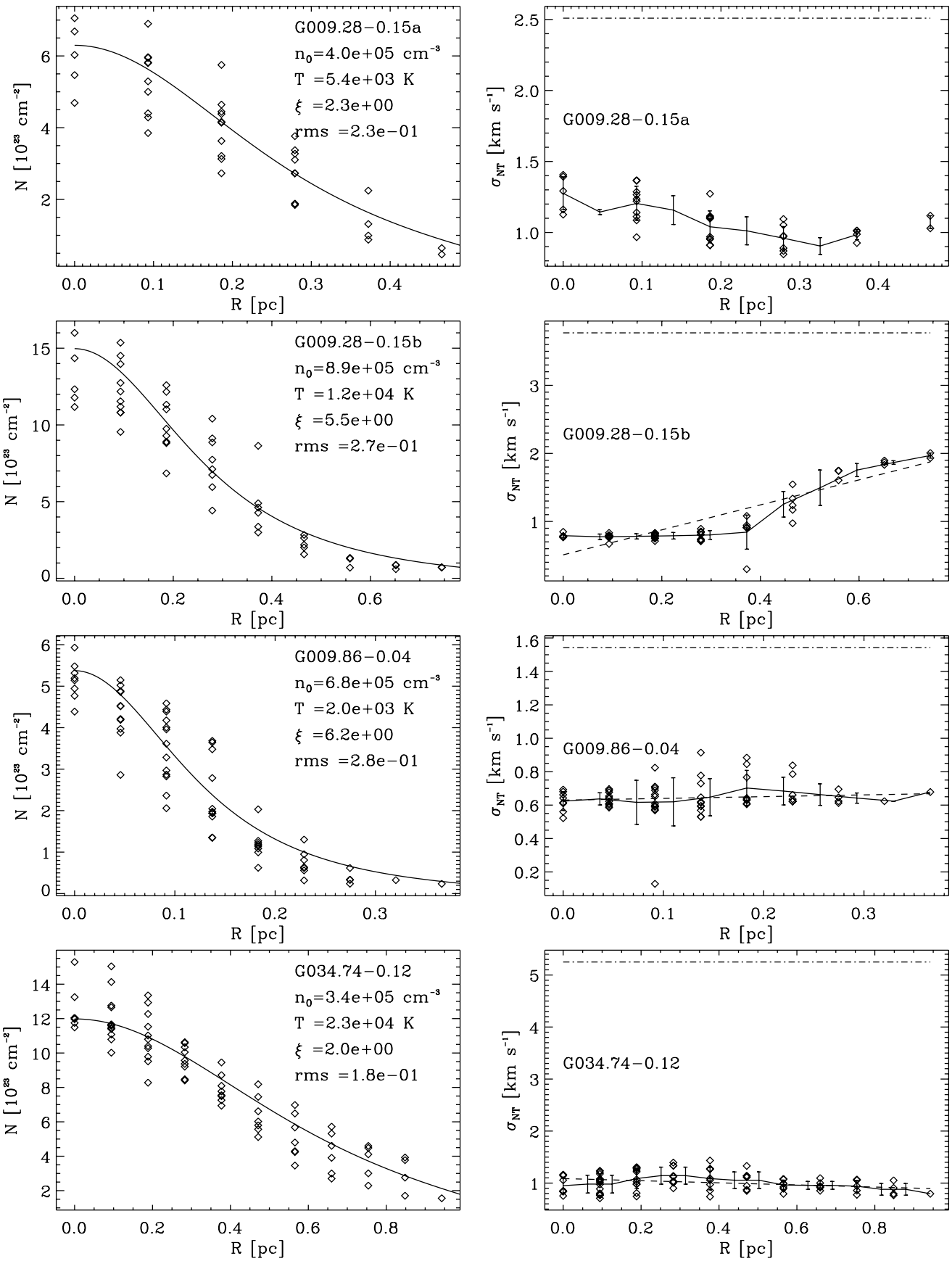

Figure 10. Left: observed column density profiles (symbols) and best fit (line) for the three "filamentary" IRDCs, with G009.28−0.15 split up in a north (a) and south (b) component. Central density n_0, isothermal temperature T_0, and the ratio of mass per unit length over critical mass ξ are indicated for each fit. Right: corresponding non-thermal velocity dispersion profiles for each IRDC (symbols). A linear regression is indicated by the dashed line, and a binned profile by the solid line including error bars. The dot-dashed constant line shows the "turbulent residual velocity" necessary to stabilize the cylinder. From the ξ-values and the difference between actual and residual dispersion we see immediately that all IRDCs are unstable.

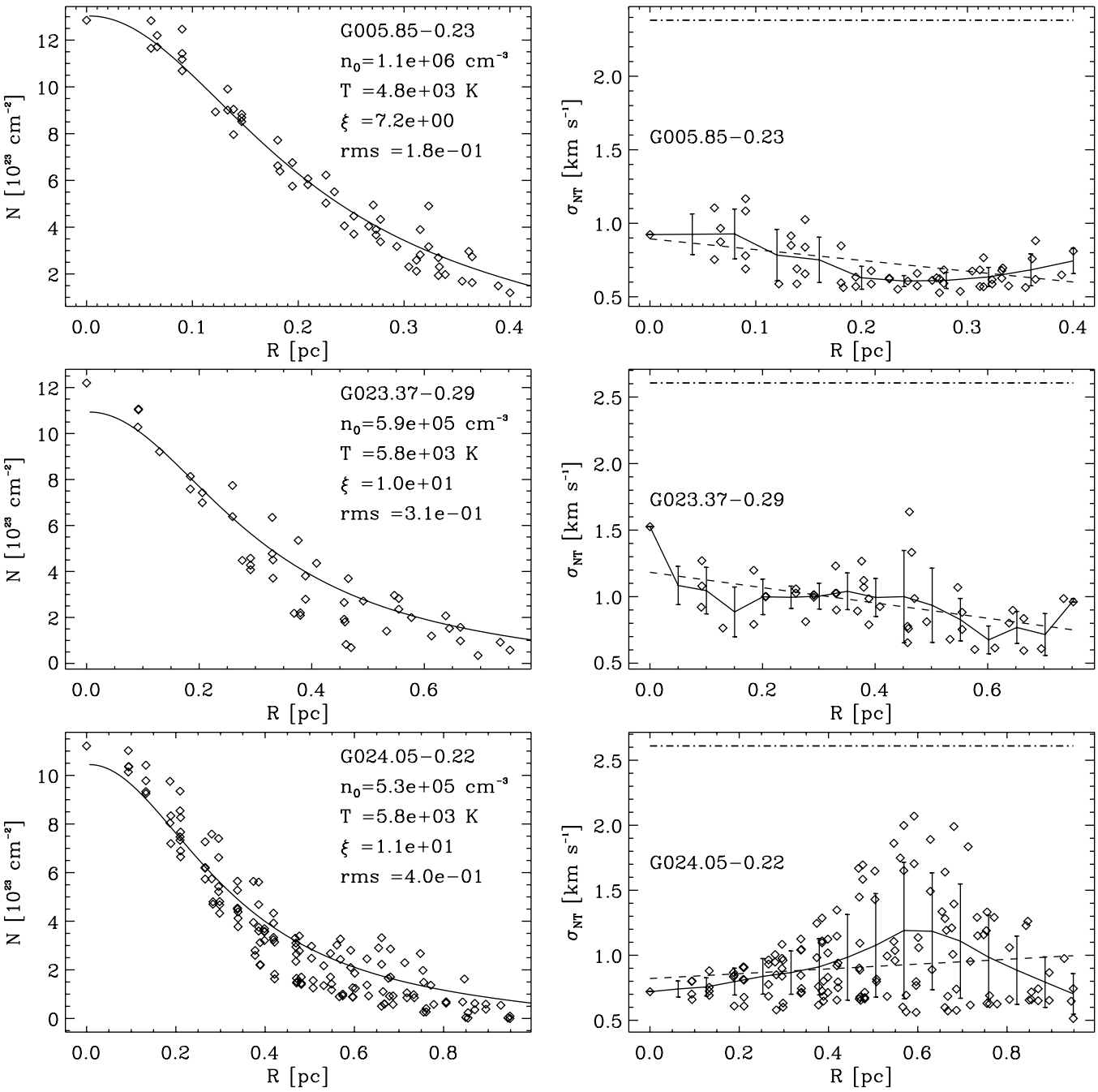

Figure 11. Left: observed column density profiles (symbols) and best fit (line) for the three "spherical" IRDCs modeled as Bonner–Ebert spheres. Central density n_0, isothermal temperature T_0, and $\xi_{\rm BE}$ are indicated for each fit. Right: corresponding non-thermal velocity dispersion profiles for each IRDC (symbols). A linear regression is indicated by the dashed line, and a binned profile by the solid line including error bars. The dot-dashed constant line shows the "turbulent residual velocity" necessary to stabilize the BE-sphere. From the ξ-values and the difference between actual and residual dispersion we see that all IRDCs are unstable.

to immediate fragmentation and, once a sufficiently high column density has been assembled, to local and global gravitational collapse. The model centroid profiles show similar asymmetries and tails as we see in Figure 9. These asymmetries arise from infall in a non-uniform medium, i.e., clumps of gas are falling into the gravitational potential well. Such events may cause the asymmetries in the observed profiles. In other words, gravitational collapse of a molecular cloud would not necessarily result in symmetric centroid velocity distributions. Further high-resolution studies, using appropriate high-density gas tracers, must be conducted in order to test our inferences about gravitational collapse in more detail.

If turbulence cannot support the IRDCs, could magnetic fields? In the absence of observational data for our IRDCs, we can estimate the critical field strengths required for cloud support. Using the expression for the critical mass-to-flux ratio for a sheet-like cloud by Nakano & Nakamura (1978), the critical field strength is given by

$$B_{\rm cr} = 0.34 \left(\frac{M}{M_\odot}\right)\left(\frac{A}{\rm pc^2}\right)^{-1} \mu{\rm G}, \quad (8)$$

with the cloud mass M, and the (projected) area A. The estimates (Table 1) are larger by a factor of a few than magnetic field strengths from CN Zeeman measurements (e.g., Falgarone et al.

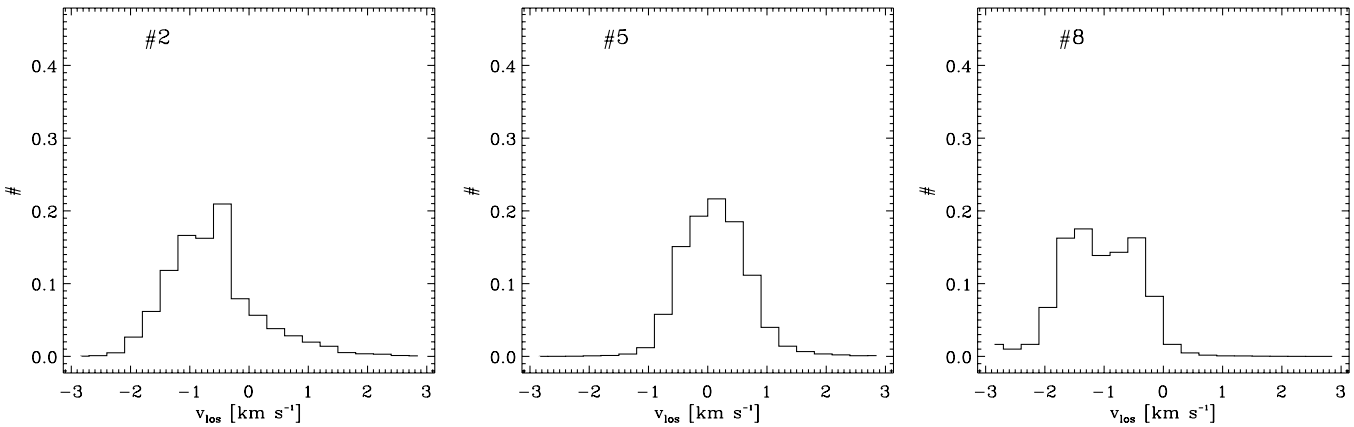

Figure 12. Normalized centroid velocity histograms of collapsing and fragmenting molecular clouds (see the text). The measurements are centered on the three most massive gravitationally bound cores (numbers 2, 5, and 8 from model Gf2 of Heitsch et al. 2008a). Asymmetries and high-velocity tails are visible similar to the observational histograms. While not proof, the consistency of distributions is suggestive.

2008; Crutcher et al. 2010), suggesting that magnetic fields are unlikely to provide wholesale support to the IRDCs, although they might be strong enough to affect the gas dynamics.

5. CONCLUSION

In this paper, we have furthered our analysis of the ammonia maps presented in Paper I, focusing here on IRDC kinematics. Our main conclusions are as follows.

1. In general, the imaged kinematic properties derived from the NH_3(1,1) line and (2,2) line are very similar and strongly corroborate each other. A notable exception is the IRDC G009.86−0.04 where the line-center velocities are offset by ∼0.5 km s^{-1} and the (1,1) linewidths are everywhere below 2 km s^{-1} while the (2,2) linewidths reach up to 4 km s^{-1}; these differences are likely due to the active cluster formation underway in this IRDC, which selectively affects slightly warmer gas traced by the higher excitation (2,2) line.
2. For all of the IRDCs with robust measurements, non-thermal motions are greater than thermal motions by factors of 2–8. The linewidths are always greater than the range of centroid velocities across the cloud. Indeed, objects of this mass are expected to be in early phases of fragmentation from turbulent molecular cloud complexes, and this phase of fragmentation is integral to setting the conditions of the massive star and cluster formation to follow.
3. The velocity fields across the IRDCs are typically very regular, showing smooth gradients in centroid velocity at the resolved size scales. These gradients could be due to rotation, shear, infall, or residual turbulent motions from the fragmentation process. Observed departures from the regular trends are generally connected to mid-infrared point sources tracing embedded YSOs. At the sites of these sources, the centroid velocity may be shifted by 0.5–1.5 km s^{-1}, perhaps due to infall onto, or outflow feedback from, protostars within the clouds. These effects tend to be greatest when a point source is detected at 24 μm only, i.e., at an early phase of star formation.
4. For all of the IRDCs, the kinetic energy estimated from the observations is insufficient to provide support against collapse. We perform basic models taking into account the projected geometry of the IRDC. This spatial analysis of the thermal, kinetic, and gravitational energy content indicates that none of the clouds are in equilibrium. Rather, the energetics combined with the density structure suggest that the clouds are in active fragmentation and collapse, in contrast to the static "turbulent core" picture outlined by McKee & Tan (2002, 2003).

The authors thank the anonymous referee for comments which greatly improved the manuscript. S.R. is grateful to Lee Hartmann and Fred Adams for useful discussions. This work was supported by the National Science Foundation under Grant 0707777. F.H. acknowledges support by NSF grant AST-0807305.

REFERENCES

Arons, J., & Max, C. E. 1975, ApJ, 196, L77
Arquilla, R., & Goldsmith, P. F. 1986, ApJ, 303, 356
Beuther, H., Sridharan, T. K., & Saito, M. 2005, ApJ, 634, L185
Bonnor, W. B. 1956, MNRAS, 116, 351
Brunt, C. M., & Heyer, M. H. 2002, ApJ, 566, 289
Brunt, C. M., Heyer, M. H., & Mac Low, M.-M. 2009, A&A, 504, 883
Burkert, A., & Bodenheimer, P. 2000, ApJ, 543, 822
Burkert, A., & Hartmann, L. 2004, ApJ, 616, 288
Butler, M. J., & Tan, J. C. 2009, ApJ, 696, 484
Carey, S. J., Clark, F. O., Egan, M. P., et al. 1998, ApJ, 508, 721
Carey, S. J., Feldman, P. A., Redman, R. O., et al. 2000, ApJ, 543, L157
Crutcher, R. M., Wandelt, B., Heiles, C., Falgarone, E., & Troland, T. H. 2010, ApJ, 725, 466
Devine, K. E., Chandler, C. J., Brogan, C., et al. 2011, ApJ, 733, 44
Du, F., & Yang, J. 2008, ApJ, 686, 384
Ebert, R. 1955, Z. Astrophys., 37, 217
Egan, M. P., Shipman, R. F., Price, S. D., et al. 1998, ApJ, 494, L199
Falgarone, E., Troland, T. H., Crutcher, R. M., & Paubert, G. 2008, A&A, 487, 247
Field, G. B., Blackman, E. G., & Keto, E. R. 2008, MNRAS, 385, 181
Friesen, R. K., Di Francesco, J., Shirley, Y. L., & Myers, P. C. 2009, ApJ, 697, 1457
Goodman, A. A., Benson, P. J., Fuller, G. A., & Myers, P. C. 1993, ApJ, 406, 528
Heitsch, F., Hartmann, L. W., & Burkert, A. 2008a, ApJ, 683, 786
Heitsch, F., Hartmann, L. W., Slyz, A. D., Devriendt, J. E. G., & Burkert, A. 2008b, ApJ, 674, 316
Ho, P. T. P., & Townes, C. H. 1983, ARA&A, 21, 239
Jackson, J. M., Finn, S. C., Rathborne, J. M., Chambers, E. T., & Simon, R. 2008, ApJ, 680, 349
Jijina, J., Myers, P. C., & Adams, F. C. 1999, ApJS, 125, 161
Johnstone, D., Rosolowsky, E., Tafalla, M., & Kirk, H. 2010, ApJ, 711, 655
Lada, C. J., Bergin, E. A., Alves, J. F., & Huard, T. L. 2003, ApJ, 586, 286
Ladd, E. F., Myers, P. C., & Goodman, A. A. 1994, ApJ, 433, 117
Maret, S., Faure, A., Scifoni, E., & Wiesenfeld, L. 2009, MNRAS, 399, 425
McKee, C. F., & Ostriker, E. C. 2007, ARA&A, 45, 565

McKee, C. F., & Tan, J. C. 2002, Nature, 416, 59
McKee, C. F., & Tan, J. C. 2003, ApJ, 585, 850
Mouschovias, T. C., & Spitzer, L., Jr. 1976, ApJ, 210, 326
Myers, P. C., & Benson, P. J. 1983, ApJ, 266, 309
Nakano, T., & Nakamura, T. 1978, PASJ, 30, 671
Ostriker, J. 1964, ApJ, 140, 1056
Padoan, P., Boldyrev, S., Langer, W., & Nordlund, Å. 2003, ApJ, 583, 308
Perault, M., Omont, A., Simon, G., et al. 1996, A&A, 315, L165
Peretto, N., & Fuller, G. A. 2009, A&A, 505, 405
Pillai, T., Wyrowski, F., Carey, S. J., & Menten, K. M. 2006, A&A, 450, 569
Ragan, S. E., Bergin, E. A., & Gutermuth, R. A. 2009, ApJ, 698, 324
Ragan, S. E., Bergin, E. A., Plume, R., et al. 2006, ApJS, 166, 567
Ragan, S. E., Bergin, E. A., & Wilner, D. 2011, ApJ, 736, 163
Rathborne, J. M., Jackson, J. M., & Simon, R. 2006, ApJ, 641, 389
Rosolowsky, E. W., Pineda, J. E., Foster, J. B., et al. 2008, ApJS, 175, 509
Sakai, T., Sakai, N., Kamegai, K., et al. 2008, ApJ, 678, 1049
Vasyunina, T., Linz, H., Henning, Th., et al. 2009, A&A, 499, 149
Vázquez-Semadeni, E., Gómez, G. C., Jappsen, A. K., et al. 2007, ApJ, 657, 870
Walmsley, C. M., & Ungerechts, H. 1983, A&A, 122, 164
Wang, Y., Zhang, Q., Pillai, T., Wyrowski, F., & Wu, Y. 2008, ApJ, 672, L33
Wiseman, J. J., & Ho, P. T. P. 1998, ApJ, 502, 676